Catena 182 (2019) 104145

Contents lists available at ScienceDirect

Catena

journal homepage: www.elsevier.com/locate/catena

SmartWood: Laboratory experiments for assessing the effectiveness of smart sensors for monitoring large wood movement behaviour

Gabriel Spreitzer[a,*], Joseph Gibson[a], Max Tang[a], Jon Tunnicliffe[b], Heide Friedrich[a]

[a] Department of Civil & Environmental Engineering, University of Auckland, Auckland, New Zealand
[b] School of Environment, University of Auckland, Auckland, New Zealand

A R T I C L E I N F O

Keywords:
Sensor-tagged large wood (LW)
Nine-degree of freedom (9-DoF) SmartWood
Measuring LW movement behaviour
Laboratory experiments

A B S T R A C T

Large wood (LW), delivered to the river channel in the course of commercial forest harvesting, or generated during natural events, can be mobilised during floods. The movement of wood along the river corridor involves complex cycles of recruitment, mobilisation, transportation and deposition. These processes are affected by the size, buoyancy, roughness and complexity of the wood components, as well as the relative spatial density and the character of the channel boundary elements. In order to understand the probabilistic behaviour of woody elements within the fluvial system, it is important to be able to characterise the timing, mechanisms and duration of the various phases of wood transport. Due to a lack of suitable sensing technology, a detailed understanding of LW recruitment, transport and accumulation processes has thus far been elusive. In this study we introduce a technique using a nine-degrees of freedom (9-DoF) sensor embedded in a 'SmartWood' dowel that shows strong potential for measuring and recording LW movement. The SmartWood assembly comprises an integrated sensor with an inertial measurement unit (IMU), accelerometer, gyroscope and magnetometer, installed in a wooden dowel that is scaled to represent a tree stem in the flume. The sensor is able to record the many different motions of LW transport. The sensor-tagged wood dowel is density-compensated, with a specific weight of 0.5 g·cm^{-3}. A series of verification and experimental tests was carried out to evaluate the applicability of this new technology for LW research and is presented herewith. Experiments were conducted in a 6.3 m long and 1.5 m wide flume with sinuous channel course and mobile gravel bed conditions, with a discharge of up to 10 l·s^{-1}. We show that LW movement during transport, particularly starting, rolling, yawing and stopping processes, but also LW impacts, can be quantified within a flume environment. These findings can be further developed to obtain the translational movement behaviour of LW, which is needed to refine probabilistic models of downstream trajectories. Understanding complex LW movement is essential for informing freshwater and forestry management guidelines.

1. Introduction

Wood is recruited to river channels via a range of natural processes, such as wind throw, bank failure (Rusyda et al., 2014), landslides and debris flows (Stubblefield et al., 2009), leading to the entrainment of large wood (LW) into a fluvial system. Large-scale forest harvesting in steep terrain may also introduce wood to the channel (Phillips et al., 2018). Once LW enters a river channel, it can be mobilised, transported and randomly deposited along channel margins. In some cases, LW may form complex accumulation structures (Fig. 1), interacting with riparian vegetation, but also river-crossing infrastructure such as bridges and weirs. Such infrastructure is a critical lifeline for rural communities, and these can be particularly vulnerable. LW impacts can lead to bridge failure, causing disruption to transport and leading to the isolation of communities (Gschnitzer et al., 2017). Thus, it is important to understand how LW movement affects channel hydraulics and morphology, and follow-on effects for infrastructure and the river ecology.

From an ecological perspective, wood budgets provide an integrated model of the flux of woody material from catchments, but we still do not understand the dynamics of entrainment, interaction with channel flow and boundaries, and final deposition, as the assessment is complex and challenging (Tonon et al., 2018). Capturing the complex movement processes of LW is difficult due to a lack of appropriate sensing technology. Airborne and field-based monitoring of environmental processes have become more popular for LW research, in order to quantify wood budgets and study wood fluxes by means of high-resolution photography (Smikrud and Prakash, 2006; Milani et al., 2018), video

* Corresponding author.
E-mail addresses: gspr390@aucklanduni.ac.nz (G. Spreitzer), j.tunnicliffe@auckland.ac.nz (J. Tunnicliffe), h.friedrich@auckland.ac.nz (H. Friedrich).

https://doi.org/10.1016/j.catena.2019.104145
Received 8 April 2019; Received in revised form 5 June 2019; Accepted 25 June 2019

Fig. 1. An exceptional example of large wood (LW) accumulation on Tapuae Stream after a storm event at a river on New Zealand's East Cape in 2017.

capture (MacVicar and Piégay, 2012; Ruiz-Villanueva et al., 2018), laser scans (Geerling et al., 2007; Richardson and Moskal, 2016; Magnussen et al., 2018), or electromagnetic tags implanted into selected logs (MacVicar et al., 2009; Schenk et al., 2014; Ravazzolo et al., 2015). These studies allow for quantification of instream wood, and determination of sites of mobilisation and deposition for individual LW pieces. However, hardly any studies are available that provide an insight into LW movement processes, downstream trajectories, transport mechanisms and the dynamic forces involved in wood mobilisation and transfer.

Understanding LW movement is important (i) for the evaluation of entrainment processes of wood into a river system, (ii) for understanding log remobilisation and transport activity (Braudrick and Grant, 2000) and (iii) for identifying 'key'-logs that tend to strike and accumulate at critical cross-sections, initiating LW accumulations and damaging river-crossing infrastructure, as well as the environment.

1.1. LW definition and processes

Wood from both natural and anthropogenic sources influences the ecology and geomorphology of a river (MacVicar et al., 2009; Ravazzolo et al., 2015). It can influence the riparian processes of erosion and sedimentation (Assani and Petit, 1995; Ravazzolo et al., 2015), as well as the ecological diversity of rivers, forming aquatic habitat and acting as a food source for organisms in the riparian environment (Gurnell et al., 2002). Previous studies have defined LW as pieces of wood with length and diameter greater than 1 m and 0.1 m, respectively (Nakamura and Swanson, 1994; Abbe and Montgomery, 2003; Wohl and Jaeger, 2009; Martin et al., 2018). In general, LW undergoes three main processes in its downstream movement: (i) recruitment and entrainment, followed by (ii) transportation in the stream channel before (iii) final deposition, the latter often involving complex accumulation processes. Typical residence times of LW in stream channels have been found to be in the order of a few years (Piegay et al., 1999) up to several centuries (Keller and Tally, 1979; Harmon et al., 1986), depending on factors such as the channel slope, floodplain width and the confinement of the valley.

Studies of wood in stream systems have found that when water depth reaches a point relative to the log diameter, buoyant LW elements will float and become primed for entrainment. This instability leads to mobilisation (Braudrick and Grant, 2001; Bocchiola et al., 2006; Davidson et al., 2015). Braudrick and Grant (2000) further postulated that entrainment is a function of four parameters, namely log length, diameter, density and orientation. Logs with an orientation perpendicular to flow direction have shown a higher probability for transport initiation (Davidson et al., 2015). A case study showed that in most native New Zealand streams, wood deposited on floodplains or bars tends to be aligned perpendicular (90°) to flow direction (Baillie and Davies, 2002). Determining the actual sequence of mobilisation processes is difficult due to a lack of applicable techniques and methodologies. For instance, there are likely to be sliding and rotational movements (Ruiz-Villanueva et al., 2016a) that contribute significantly to log entrainment, though these mechanics are poorly understood. Improving our knowledge of mobilisation processes can help in developing probabilistic - or even mechanistic - models of log recruitment.

LW is transported downstream during high flow events, normally in the rising limb of the hydrograph (Ravazzolo et al., 2015), with increasing flow depth. Braudrick and Grant (2001) found that LW is generally transported along the centreline of a stream and is aligned parallel with the flow, however, interactions with other floating LW, embankments and in-stream bars may disturb parallel and centred movement, adding more complexity to transport processes and downstream trajectories. It has been found that as wood volume in transit increases, transportation generally decreases, owing to congestion of woody elements (Ruiz-Villanueva et al., 2016b). Movement of LW en masse becomes a probabilistic problem, and therefore more estimates of transit times are needed to develop adequate models for the bulk transport of riverborne wood.

We know that deposition generally occurs on the river bed or on bars in low flow conditions, often in areas with high roughness (Wyżga et al., 2017). Individual logs, once deposited, tend to collect even more LW and consequently one well-lodged wood element can become the nucleus for a large jam. There is clearly a complex relationship between river stage, buoyancy of a given wood mass, and the snagging of branches or rootwads with immobile boundary elements (including other deposited wood).

1.2. Remote sensing of LW

LW in the riparian environment is a widely researched topic, with studies having been undertaken both in situ (MacVicar et al., 2009; Ravazzolo et al., 2015; Ruiz-Villanueva et al., 2016b; Wyżga et al., 2017) and in the laboratory environment (Rusyda et al., 2014; Davidson et al., 2015; Gschnitzer et al., 2017). Some of these studies have looked at the use of sensors, in the form of radio-frequency identification (RFID) tags to help understand LW movement, but these are limited in their application as they only provide information about where LW started and finished its journey (MacVicar et al., 2009; Ravazzolo et al., 2015; Wyżga et al., 2017). Research in areas other than LW, such as debris transported through tsunamis (Goseberg et al.,

2016) or in geotechnics and fluvial geomorphology (Hiller et al., 2014; Olinde and Johnson, 2015; Gronz et al., 2016; Valyrakis and Farhadi, 2017) has also applied RFID and sensors. There have been tremendous advances and insights offered from these sensor-tagged tracer studies that help to better understand the transfer of wood, debris and sediment through various environments. Fluvial tracer studies have demonstrated that smart sensors can be effectively used to characterise the probability functions for entrainment, movement modes, deposition and rest times between transfer episodes.

Olinde and Johnson (2015) used active smart pebbles equipped with an accelerometer unit for particle tracking, and reported difficulties in differentiating between real movement process and clast rocking in place. Sensors that track orientation and position in three dimensional space with great accuracy are not suitable for many applications due to the extreme cost or inappropriate size (Ahmad et al., 2013). Motion can be tracked with inertial measurement units (IMUs), which are low cost, low processing power and compact orientation sensors. These have been applied in a variety of research areas, including medical rehabilitation, sports analysis and animal behaviour analysis (Ahmad et al., 2013; Aldoumani et al., 2015). Due to forces from motion (accelerometer), changes in angular velocity (gyroscope) and magnetic field (e-compass, magnetometer) position and orientation in all three-dimensions can be estimated over time (Ahmad et al., 2013; Fischer et al., 2013; Goseberg et al., 2016). The ability to measure body-frame rotations, as well as force energies, makes these types of sensors useful for hydraulic research and LW tracking.

Despite the successful implantation of the sensors mentioned above, there are challenges in using the obtained information for accurate translational and rotational motion tracking. Orientation can be represented through the use of Euler angles or quaternions (Fischer et al., 2013; Aldoumani et al., 2015). Euler angles of roll, pitch and yaw (Fig. 2) are commonly used, as they provide an intuitive representation of orientation, however they are prone to errors, such as the issue of 'gimbal lock' (Madgwick et al., 2011). Gimbal lock refers to a problem of axis parallelism, when at least two of the three gimbal axes align to a single plane, resulting in the loss of one degree of freedom (Hoag, 1963). These same issues do not apply to quaternions (Madgwick et al., 2011). Smart sensors allow the visualisation of orientation and movement of LW as they are transported, without the need for constant visual contact. Position estimates can be found through the integration of acceleration values through time, similar to the process of dead reckoning commonly used in pedestrian tracking, following the rotation of the sensor body frame to the global frame (Fischer et al., 2013). Each integration calculation introduces a new component of drift error, typically resulting in large discrepancies between observed and calculated results (Ahmad et al., 2013). There are a number of algorithms available to suppress the drift in orientation using mathematical formulas (Madgwick et al., 2011; Liu et al., 2018), however, these algorithms work as a filter using a specific threshold value with the aim of gait pattern tracking. This means that after each step, the sensor registers a period of signals showing very few deviations, which suggests that the object is at rest. Thereupon, the algorithm detects the touchdown on the ground and keeps orientation computations static, which limits the drift, until threshold-exceeding signals are registered.

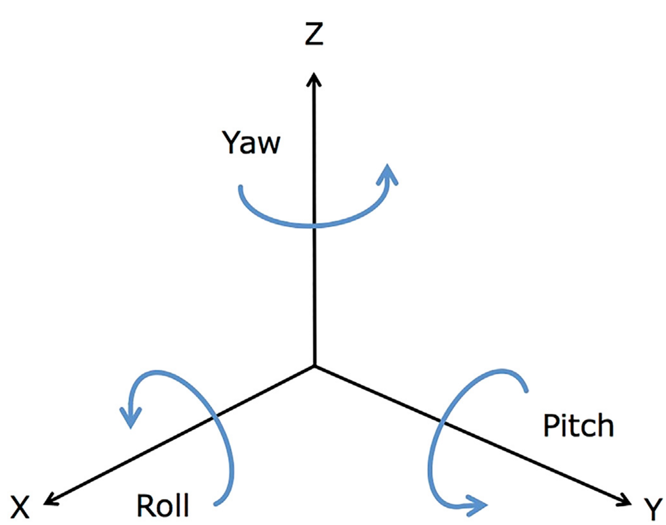

Fig. 2. Roll, pitch and yaw as a frame for orientation.

Apart from using accelerometer data to estimate position and orientation, the sensor readings from the accelerometer can be used for recording impact forces (Goseberg et al., 2016). There have been major advances in measuring impact forces using IMU's, most notably in medicine (Worsey et al., 2019) and in the automotive industry, recording crash tests (Xu et al., 2018). Changes in acceleration continuously occur for LW through interaction with channel boundaries and river-crossing infrastructure, but also due to wood-wood interaction processes and changes in flow hydraulics. Measuring the magnitude of these accelerations allows researchers to determine the impact forces of LW in transit.

1.3. Objectives

This study focused on the suitability of using the new smart sensor technology to monitor the movement behaviour of LW in a scaled gravel bed river in the laboratory. It was essential to interpret and verify smart sensors data using video capture, in order to accurately and independently track the movement of scaled LW in the flume. The sensors are capable of measuring acceleration, angular velocity and magnetic field strength for all three dimensions - nine degrees of freedom (9-DoF). They were implanted into wooden dowels (scaled LW), to be used in the laboratory flume. To our knowledge this type of smart sensor has not been applied to this area of LW research previously.

Our objectives were:

(i) to evaluate state-of-the-art smart sensors for application in LW research in a wet, turbulent and impact-prone environment for a variety of criteria, including water-proofing, power consumption, memory, data transfer, sensor control, and shock-resilience, and
(ii) to assess the capability of the sensors for quantification of LW movement behaviour in the flume, considering mobilisation, transport and deposition processes, given the constraints of recording frequency (resolution) and data processing for position and orientation estimates, using independent measurements.

9-DoF sensor data results of LW rotational and translational movement during transport are discussed in relation to our currently limited understanding of LW transport processes.

2. Experimental setup

A hydraulic flume representing a characteristic New Zealand gravel-bed river was set up in the Hydraulic Engineering Laboratory at the University of Auckland to perform LW experiments. The flume is laid out as a sinuous channel with live-bed conditions and fixed embankments. The entire experimental setup is scaled at a ratio of 1:15, including bed materials, wooden elements and discharge rates. The channel ranges in width from 0.8 to 1 m, over a length of 6.3 m with a gradient of 0.02 (Fig. 3). Bed material is a mixture of angular gravel (4 to 63 mm), and the immobile lateral channel boundary is covered with an 8 to 16 mm gravel and cement mixture. The relatively coarse gravel material is representative of cobbly material, with rough prototype channel elements, such as boulders up to 1 m in diameter. Wood dowels with a length of 267 mm, and 22 mm in diameter, were used to simulate LW elements in the flume, representing wood log dimensions of 4 m in

Fig. 3. Custom-designed hydraulic flume for LW research at the University of Auckland, New Zealand (a). Three-dimensional Structure from Motion (SfM) model of the flume channel (b).

length and 0.33 m in diameter. This scaling is consistent with standard logs cut in timber production and represents the simplest realistic case of wood introduced to the channel, which reduces the complicated effects of branches and rootwads. Flow rates in the flume are controlled via electro-magnetic valve and can range up to 75 $l \cdot s^{-1}$, which is representative of a flood event with a magnitude of 60 to 80 $m^3 \cdot s^{-1}$ for a prototype catchment roughly 100 km^2 in area. A bridge with a pier in the centre of the channel is installed 4 m downstream from the inlet, simulating a 'one-lane' river crossing with prototype dimensions of 22.5 m in length and a width of 3.6 m. The installation of a video camera above the inlet of the flume, with a view in the downstream direction, enables recording of the experiments.

The 9-DoF smart sensors were inserted into the centre of the cylindrical wooden dowels (Fig. 4a), similar to those used by Braudrick and Grant (2001), Rusyda et al. (2014) and Gschnitzer et al. (2017). It was assumed that the average density of wood logs encountered in the riparian environment would be equal to 0.5 $g \cdot cm^{-3}$, consistent with *Pinus radiata*. *Pinus radiata* is a softwood of medium density that is widely planted throughout New Zealand. This is the same density as used by Braudrick and Grant (2000). Three sensors were deployed to assess experimental variation in the data; however, we show results for only one of the sensor-tagged dowels, for clarity.

Each dowel was hollowed out, with a 10 mm diameter hole bored through the full length of the dowel (Fig. 4b). The sensor was then gently pushed into the hollowed dowel so that it was located exactly in the centre. The sensor density was estimated to be 1.75 $g \cdot cm^{-3}$. To ensure that the sensor-tagged wood dowels maintained an overall 0.5 $g \cdot cm^{-3}$ density, holes of 12 mm in diameter and 80 mm in depth were bored into either end of the dowel to shed some further weight.

To allow for the wood dowels to be easily identified, they were painted with different colours. To restrict water entry and to ensure easy removal and insertion of the sensors, wool was used to partially fill the holes, and polyurethane (PU) foam was used to close off the ends of the dowels. Finally, the ends of the sensor-tagged dowels were sealed using hot-melt adhesive.

Specific features (Table 1) of the 9-DoF smart sensors (Fig. 4c) make them well-suited to LW research applications. The IMU casing is watertight and includes a 1.6 V, 600 mAh battery, enabling multiple hours of usage. The cylindrical form of the dowels is amenable to housing the sensor. A wake-up function automatically starts measurement once the sensor-tagged wood dowel experiences motion (vibration). When no motion is registered the sensor stops measuring by switching to stand-by mode in order to save memory. Our smart sensor unit is equipped with Wi-Fi, using the 915 MHz frequency band, allowing live communication over a range of 100 m during experiments, and memory download, even when still inserted in the wooden dowels. Measurements were obtained from the accelerometer, gyroscope and magnetometer at a sampling frequency of 100 Hz. Internally, the accelerometer operates at 1600 Hz, the gyroscope at 3200 Hz and the magnetometer has an upper limit of 300 Hz for data collection. All output data are time synchronized and saved in raw as well as .csv format on an internal 2 MB flash memory. At a measuring frequency of 100 Hz the accelerometer data show a maximum noise signal of 1.5 mg, for each channel (axis). The noise range for the gyroscope at the same frequency is 0.04 $deg \cdot s^{-1}$ rms (root mean square) and for the magnetometer it is about 2 μT.

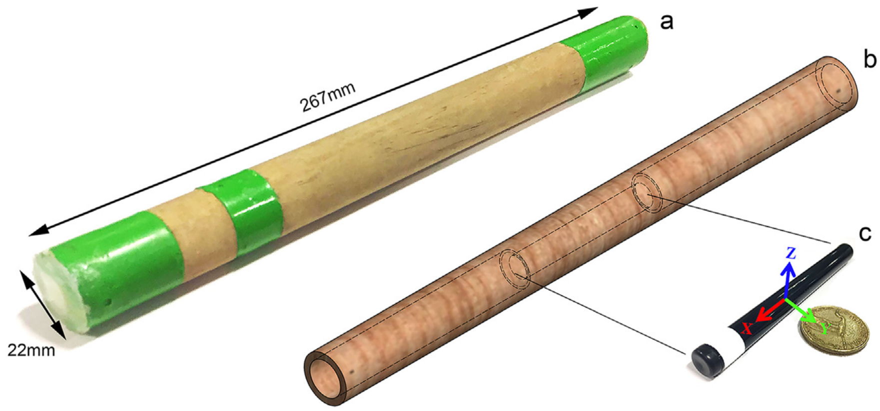

Fig. 4. Sensor-tagged and scaled SmartWood dowel (267 mm long, 22 mm diameter), individually coloured for the hydraulic flume experiments (a). Sketch of the SmartWood dowel (b), showing the hollow, 10 mm central shaft for installation of the smart sensor and the filled (density-compensated) cavities on both ends. The 9-DoF smart sensor consisting of IMU (accelerometer, gyroscope, magnetometer, on-board memory and battery) implanted in a cylindrical housing, 105 × 10 mm, with a NZD $2 coin for scale (c). The ends of the SmartWood dowel are sealed using PU-foam and silicone.

Table 1
Smart sensor specifications.

Sensor detail	Specification
Length	105 mm
Diameter	10 mm
Battery	1.5 V, 600 mAh
Lifetime	2.5 h to 10 years
Frequency	12.5, 25 and 100 Hz
Memory	2 MB
Accelerometer	0.5 mg to 16 g
Gyroscope	0.1 to 2000 deg·s^{-1}
Magnetometer	0.3 to 1300 μT
Temperature	0.01 °C
Stop recording	1 s
Wake-up	1/100 s
Communication	Wi-Fi/USB
Wi-Fi frequency	915 MHz for NZ
Operation system	Windows 7, 64-bit

3. Methodology

3.1. Verification tests

Verification was required to ensure that all sensors produce similar outputs and are adequately oriented, as well as balanced, inside the IMU. This involves independent parameter testing for each of the measuring units (accelerometer, gyroscope and magnetometer), to ensure the output data match the sequence of physical events. Acceleration, angular velocity and magnetic field were tested along three axes, using a combination of different apparatus for axes isolation. A drop test, dropping the sensors three times, was used to verify the acceleration readings of the sensors. A drill rotation test, where the sensors underwent three sets of three full rotations at a predefined constant speed, was used to test the gyroscope and magnetometer readings of the sensors.

For the drop test, the 75 mm freefall of the sensor was guided by a hollow vertical steel tube, 5 mm wider than the diameter of the sensor (Fig. 5a & b). The bottom was cushioned with a piece of rubber to protect the sensor and stop it bouncing when it impacted the base of the drop test apparatus. As this system can only measure acceleration along one axis, the x-axis, another drop apparatus was constructed to measure acceleration in the remaining two axes, y and z. Here, the sensor was lifted on a platform to a marked height of 150 mm (Fig. 5d), to be released and fall down, impacting on the bench (Fig. 5e). The different axes were measured by rotating the sensor so that acceleration in the y and z-axes of the sensor (rotation of 90°) could be measured. In order to achieve good verification results and negate additional acceleration, the platform was lifted over an interval of 10 s to the test elevation.

Both gyroscope and magnetometer data were captured using the same apparatus (Fig. 5c & f) for verification. The apparatus consisted of a hand drill, held in a vice, with an integrated speed dial that controlled the speed of drill rotation. Verification of the x-axis was performed using a vertical-facing drill, whereas for y and z-axes a horizontally positioned drill was required. The sensor was therefore attached in a specially designed console holder, so that the different axes could be isolated with respect to Earth's gravity of 9.81 m·s^{-2} or 1 g, according accelerometer reading. Each rotational measurement was kept to three rotations, with pauses of 5 s in between. The rotational velocity was kept in a range of 75 to 100 deg·s^{-1} via the speed dial.

For rotational motion, the axis symmetry of the measuring units enabled a combination of gyroscope and magnetometer verification tests. Results of rotational verification tests could be plotted together, for each individual axis, in the x, y and z directions. Raw sensor data are displayed in Fig. 6c & e; Fig. 7a, c & e on the left hand side, each starting with measured ‘Sensor Data from Gyroscope’, indicating the angular velocity in degrees per second (deg·s^{-1}) in the top graph, followed by ‘Sensor Data from Accelerometer’ in g-force (g), and ‘Sensor Data from Magnetometer’ revealing the magnetometer flux in microtesla (μT) over time in the bottom graph. Euler angles are displayed on the right hand side of the figure, as a measure of orientation with respect to a fixed coordinate system in degrees (deg) over time (s) for roll, pitch and yaw (Fig. 2). A tendency for sensor readings to ‘drift’ was expected throughout data processing (Madgwick et al., 2011). Drift, for our purposes, is defined as the time-dependent deviation between measured signal and real movement, which occurs during integration of raw sensor data. These deviations become obvious during periods of idle sensor position, and are difficult to determine for periods when the sensor is in motion.

3.2. Experimental tests

Experimental data were generated using the SmartWood dowel that was mobilised and transported downstream by flow. Flow rates were gradually ramped up from 4 to 10 l·s^{-1}, sufficient for the mobilisation and transport of the sensor-tagged dowel. At a predefined cross-section, 3 m upstream from the bridge section, the SmartWood dowel (Fig. 4) was placed in the channel centre, set at a predefined angle relative to the flow direction, specifically 0°, 45° or 90°. Dowels were placed carefully with positive z-axis facing up, and the x-axis facing downstream. Only a single SmartWood dowel was placed and tracked at a time. Discharge at the outset was a base discharge of 4 l·s^{-1}. The sensor was set to measure all nine sensor channels at a frequency of 100 Hz. Simultaneously, a camera recorded the dowel's movement. The discharge was increased to 10 l·s^{-1} (a flood event of roughly 9 m^3·s^{-1} in our prototype channel) over a period of 10 s, entraining the SmartWood dowel and transporting it downstream. After passing the bridge, the SmartWood dowel was collected at a wood retention screen installed within the outlet structure of the flume. At this point, the measurement ended, the discharge was decreased to base discharge, the memory was

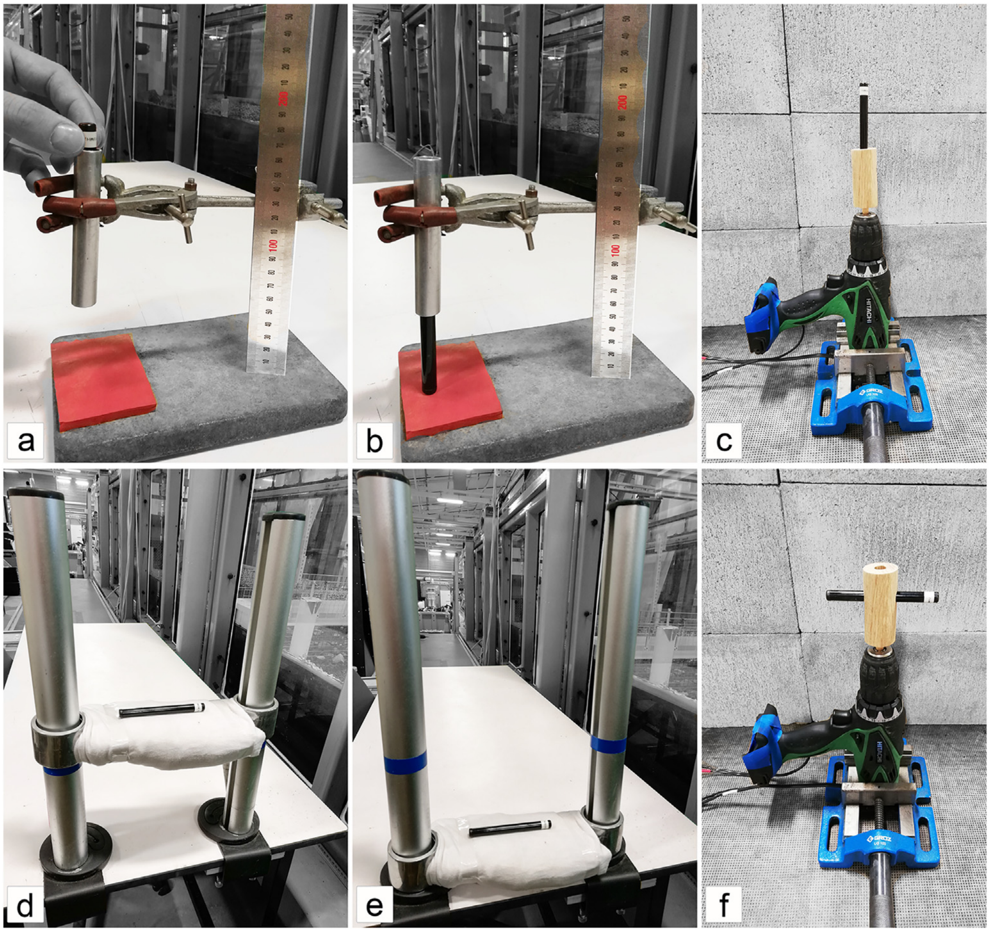

Fig. 5. Setup for Smart Sensor verification in the laboratory, consisting of a vertical drop test (a, b), from a height of 75 mm onto a rubber layer (red), in order to measure acceleration along the longitudinal axis of the sensor. (c) Rotational test for assessing gyroscope and magnetometer performance, aligned to the longitudinal x-axis. (d, e) For verification of the acceleration along the vertical z- and lateral y-axes of the IMU, a platform is used to simulate drop tests from a height of 150 mm. A rotational test, shown in (f) allows for verification of angular velocity and magnetic field strength around y- and z-axes. (For interpretation of the references to colour in this figure legend, the reader is referred to the web version of this article.)

read out and the camera was switched off.

3.3. Data analysis

After each test, memory was read for further processing in Matlab. As the sensors contain an inbuilt digital filter, the only pre-possessing that was necessary was to smooth the magnetometer readings which exhibited noise, most likely due to the presence of metal in the flume and laboratory environment. Quaternions were used to estimate the orientation of the sensors. An Attitude and Heading Reference System (AHRS) was used to output these quaternions, and convert them to Euler angles so they could be intuitively displayed (Madgwick et al., 2011). The AHRS algorithm designed by Madgwick et al. (2011) was further used to counteract the potential effects of gimbal lock. This process combines integrated gyroscope readings with acceleration and magnetometer readings to estimate orientation, which is then plotted, to allow novel insights into LW movement behaviour. Without the gyroscope and magnetometer information it was very difficult to distinguish between movement in the downstream direction and rocking in place, either from particle impacts or water turbulence (Olinde and Johnson, 2015).

4. Results and discussion

All measurements were obtained using the same SmartWood dowel for verification and experimental tests. Each test used about 0.2% of the available internal memory. Battery lifetime was clearly adequate, as no change of battery was required for the entire experimental series, with a remaining capacity of more than 30%. Reading of memory and program upload for the next tests took one to 3 min; most of this time was dedicated to establishing the Wi-Fi connection to the SmartWood dowel, which was located within a range of five meters. A check of the deployed sensor unit at the conclusion of the experiments revealed the integrity of the unit was not compromised by water or impacts.

4.1. Sensor verification

Verification tests for isolated axes were conducted to determine acceleration, angular velocity, as well as magnetic flux for x, y and z-axes. No concurrent rotations around y and z-axis were recorded in the raw data for the longitudinal x-axis (Fig. 6a), due to locking the DoF along this axis. However, for each drop (seconds 2, 13 and 26), a spin around the x-axis, indicating rotation, was recorded with the gyroscope. This rotational signal was caused by the impact upon the bottom of the drop apparatus, when the sensor rebounded upward, slightly, introducing a spin around the x-axis. The rotation stopped once the sensor converted the kinetic energy gained during free fall and remained still. The observed fluctuating signal, which was measured in-between the drops, was generated while manually resetting the sensor to its original starting position. The rubber layer at the bottom of the drop-test apparatus reduced bouncing of the sensor, allowing for clearer verification results.

The impact forces measured by the accelerometer in a positive longitudinal direction were captured at 100 Hz frequency. Impacts reached a value of 9 to 10 times the Earth's gravitational force g. A slight signal was registered on the y and z-axis channels, generated due to contact with the guiding tube after impact at the bottom.

Changes in magnetic flux, in Fig. 6a - bottom chart, were discernible during the drop, as the sensor unit fell through the steel pipe (Fig. 5a & b). When resetting the sensor to its starting position, moving it back up

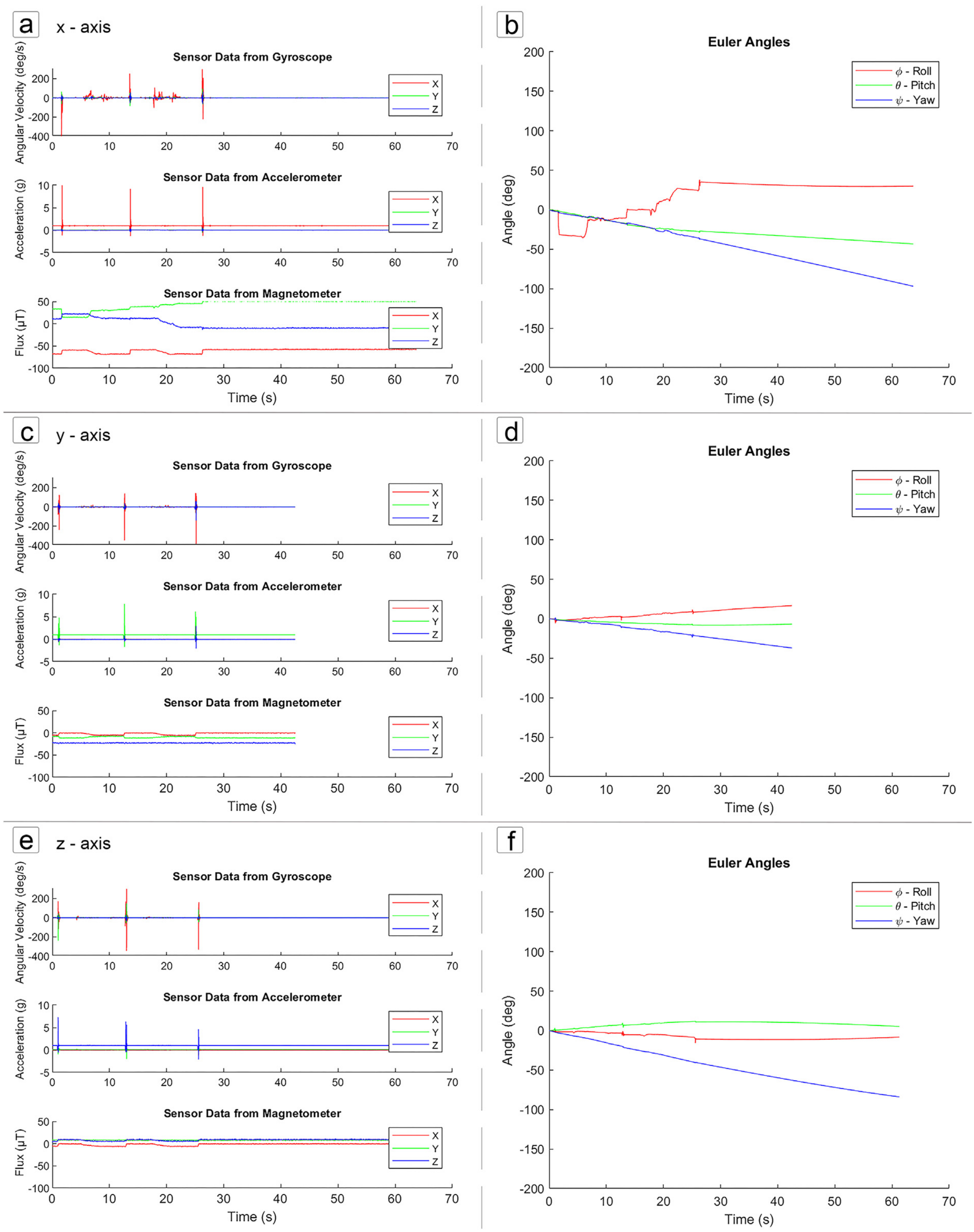

Fig. 6. Sensor data for drop test along the longitudinal x-axis, with raw data (a) and Euler angles transformation output (b), the lateral y-axis (c, d), and the vertical z-axis (e, f).

the steel tube, the magnetic field strength also changed back to its original readings. This indicates reliable and accurate raw data measurements. Euler angles were computed (Fig. 6b) and roll readings show the spin imparted by the impact, in terms of absolute orientation. The two locked y and z axes did not experience significant acceleration force; however, a constant drift over time for pitch and yaw was observed when referring to the Euler angles.

Verification tests for the remaining two axes, y and z respectively, show similar results, with the exception that impact forces are lower. The effect of lower impact forces, which are in the range of 5 to 8 g (Fig. 6c & e), is due to the guided platform which was dropped on the bench. The guiding piles on the left and right side caused friction, which resulted in lower impact forces, although the drop height increased to 150 mm. However, for both axes, similar results were

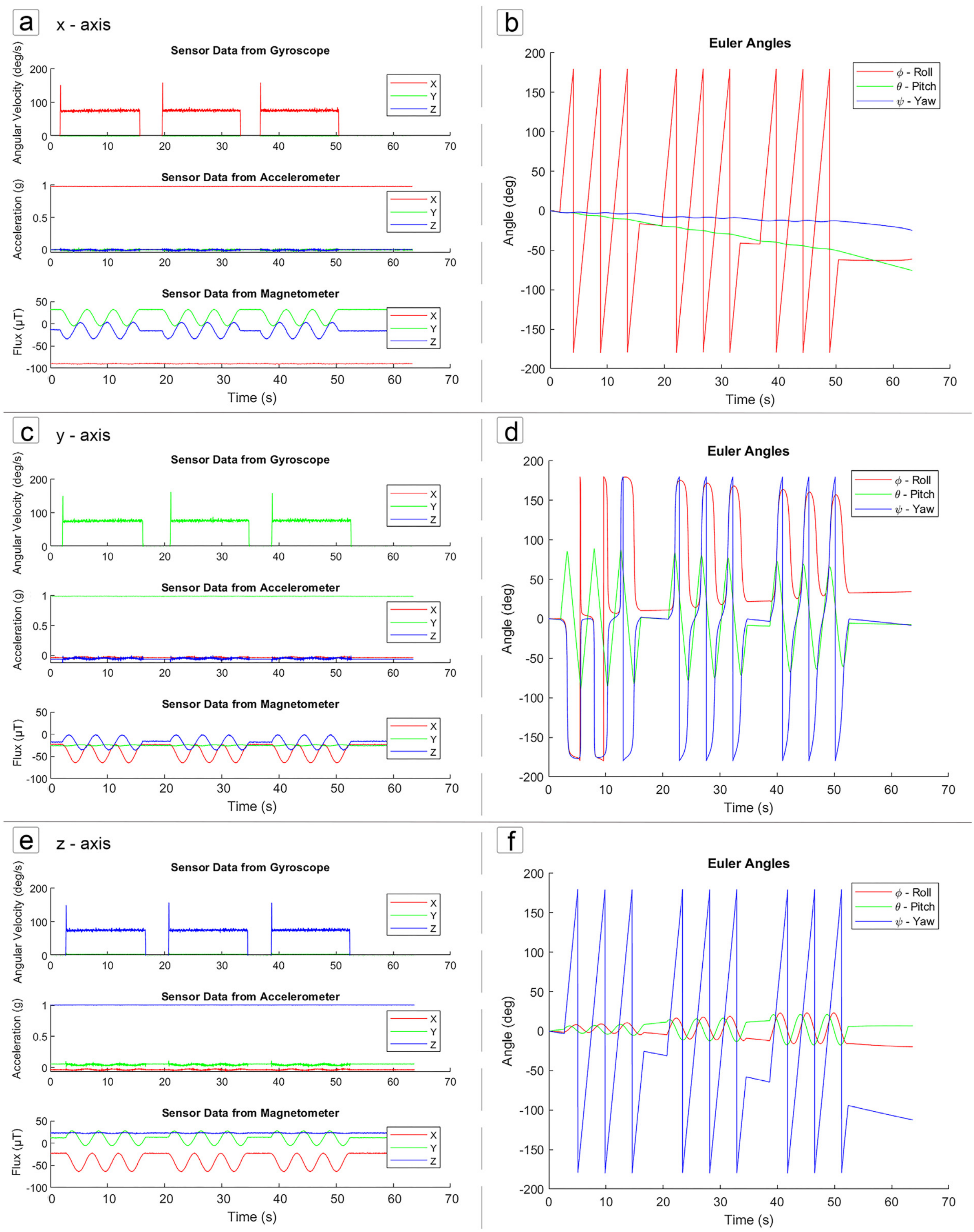

Fig. 7. Sensor data for gyroscope and magnetometer verification test around the longitudinal x-axis, with raw data (a) and the transformed output expressed as Euler angles (b), the lateral y-axis (c, d), and the vertical z-axis (e, f). (For interpretation of the references to colour in this figure, the reader is referred to the web version of this article.)

achieved. As observed previously with the drop test along the longitudinal axis, a peak signal in angular velocity was measured at the time of impact. No further significant angular velocity was measured for the axes which were tested. As the data show, a slight acceleration signal was introduced, with a maximum of 3 g, in the z-axis at the third drop test (second 25 in Fig. 6c). Axis alignment was done very carefully, however, slight displacements and differences from the ideal axis orientation resulted in a measurable signal on the remaining axes. Our results indicate the effect of this on slight displacements observed during the second and third drop test, resulting in an acceleration signal on the originally locked z-axis, although the smart sensor unit was fixed to the platform. The verification test for the z-axis (Fig. 6e) performed

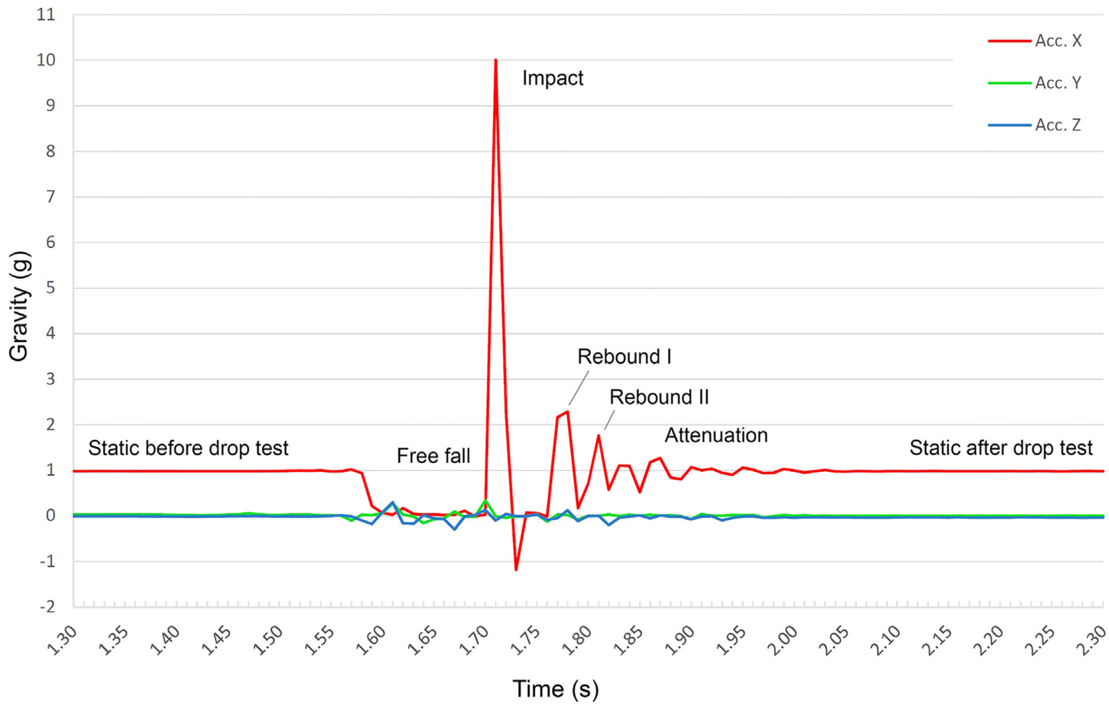

Fig. 8. Drop test impact along longitudinal direction (x-axis) - high resolution (100 Hz) over a period of 1 s – unfiltered raw data for acceleration as read from the smart sensor. The interval from 1.65 to 1.85 s shows the last milliseconds of (i) free fall measurements, (ii) the impact, (iii) the first rebound after impact, (iv) the second rebound after impact and an early stage of the attenuation phase.

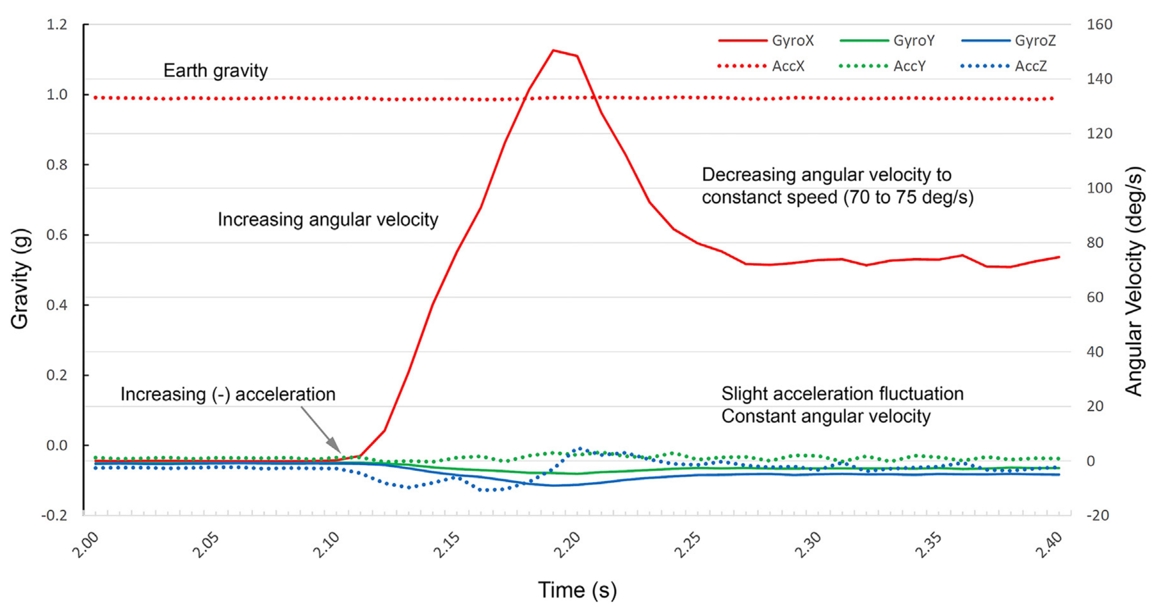

Fig. 9. Verification of angular velocity – a high resolution portion of the record for tests along the sensor's x-axis.

similarly. Measurements obtained with the magnetometer show corresponding results for both drop tests in y and z direction. In comparison to the drop test along the longitudinal axis (through the steel tube), a reduced effect on the magnetic flux was observed. The computation of Euler angles for drop tests along y and z-axis shows similar results with continuous drift and small signal changes at the time of each drop.

Fig. 8 shows a drop test for longitudinal x-axis (second 2 in Fig. 6a), demonstrating measurement resolution. As the smart sensor unit was released, gravity reduced to zero for the free axis (seconds 1.58 to 1.70), followed by the impact at the bottom of the drop test apparatus (seconds 1.70 to 1.75). At the impact, gravity reached a maximum of 10.01 g in the positive direction and when bouncing back for the first time a maximum negative acceleration of −1.18 g (second 1.73). The first rebound resulted in a positive maximum of 2.29 g, and before returning back to 0.17 g. The second rebound reached only positive maximum of 1.77 g, and a minimum of 0.58 g. Altogether four major bounce back cycles with subsequent attenuation were registered, before the sensor reached an almost stable condition. The whole rebound process only took about 0.23 s and was strongly influenced by the rubber layer at the bottom of the drop test apparatus, controlling acceleration forces. The remaining isolated axes, y and z respectively, showed hardly any acceleration, as expected. The drop scenario shown in Fig. 8, in a more highly resolved time series, only takes about 0.44 s. This dataset provides a good example of the full resolution of the smart sensors, similar to datasets produced in experimental studies on free-fall drop tests of portable products by Tempelman et al. (2012).

Verification tests for rotational movement required only one test per axis due to axis symmetry. The verification tests, intended to appraise rotational movement around all three axes, revealed identical results for each of the isolated axes (Fig. 7). Gyroscope readings consistently showed (i) an increase in angular velocity once the rotational test started, (ii) almost constant angular velocity during rotational movement, and (iii) a drop to zero when movement stopped. Turning on the drill resulted in a peak of angular velocity of 150 deg·s^{-1} at the beginning of the movement, which then decreased by approximately 50% to a continuous angular velocity in a range of 70 to 75 deg·s^{-1} over the remaining period of rotational motion. A detailed analysis of the onset of rotational movement (second 2 in Fig. 7a) reveals a sharp spike in acceleration (nearly double subsequent values), as the angular velocity increased to its peak value (Fig. 9). As angular velocity settled to an almost constant velocity (while in motion), data from the accelerometer dropped back to the initial value. This can be observed for every single rotation event. Each of the three rotational tests took about 15 s for three 360° rotations. A fluctuating acceleration signal in a range of ± 15 mg was observed during rotational movement, whereas angular velocity showed ± 2.5 deg·s^{-1} fluctuations. Acceleration signal for the tested axis showed a constant gravitational force of 1 g, indicating that the verified sensor axis faced straight upwards. Accelerometer values for the remaining axes were low because the sensor unit was located at the centre of axis rotation. Measurements of the magnetic flux were constant for the axis under consideration, however, there was a phase shift of 90° amongst the remaining axes. A sinusoidal signal, with varying amplitude of magnetic flux, was displayed as the sensor rotates within the Earth's magnetic field.

The computed Euler angles showed three full rotations for each of the axes, corresponding to the real rotational movement. The remaining locked axes were close to zero. Some drift was apparent, which influences the starting and ending position for the following verification cycle of rotational movement. For rotations around the longitudinal axis, drift of ~15° could be observed after each rotational set (3 × 360°). Pitch, the rotation around the y-axis (green in Fig. 7d), was shifted by 90° to roll and yaw, however, still indicating rotation of 360°. Our results show ~30° drift over the entire verification test for pitch, resulting in 10° of drift for each set of rotational movement. Euler angles for rotation around the vertical z-axis (Fig. 7f), show almost twice the drift as that observed along the longitudinal axis. Around the z-axis, every set of rotational movements is running short by approximately 30°, resulting from a 10° drift during every single rotation (Table 2). Total drift represents the sum of errors accrued in each of the three dimensional Euler angles (Yin et al., 2018) when integrating angular velocities for each time step (Kok et al., 2017). The observed issue of drift could limit the estimation of accurate three dimensional movement trajectories; e.g. when the sensor tagged dowel comes to rest, and the software algorithm continues with the computation due to the drift component.

Verification tests for the lateral y-axis and vertical z-axis showed similar results, and the trends observed in each test were almost identical. Accelerometer and gyroscope readings could be reliably used to detect and measure movement types, and the magnetometer was found to achieve good accuracy. The sensitivity of the sensor was sufficient to accurately capture the types of movements that were anticipated to arise in the course of LW transport in the flume. Overall, the results of the verification tests corresponded very well to the real movement sequence and our expectations. No limitations in raw data generation were found, and the experimental data collection in the flume could be started.

Table 2
Drift estimates for roll, pitch and yaw according plotted Euler angle computations.

Orientation	Roll (°)	Pitch (°)	Yaw (°)
360° (15 s)	5	3	10
3 × 360° (32.5 s)	15	10	30
9 × 360° (50 s)	45	30	90

4.2. *Experimental results*

A SmartWood dowel (Fig. 4) was placed with an angle of (i) 90°, (ii) 45° or (iii) 0° to flow direction, in the centre of the flume channel. In the course of ramping the discharge from a base discharge of 4 l·s^{-1} up to 10 l·s^{-1} our SmartWood dowel was mobilised with increasing water depth (Ravazzolo et al., 2015), and transported downstream, showing in some sequences parallel alignment with the flow and more complex movement processes during and after interaction with channel boundaries (Braudrick and Grant, 2001). The SmartWood dowel provided thereby novel data for the quantification and assessment of LW movement behaviour.

4.2.1. *90° alignment*

The first experiment was carried out using a SmartWood dowel placed with an orientation perpendicular (90°) to flow direction. A camera captured all experimental tests as illustrated in Fig. 10. With increasing discharge, the SmartWood dowel started movement. The sensor data from the gyroscope registered an increase in angular

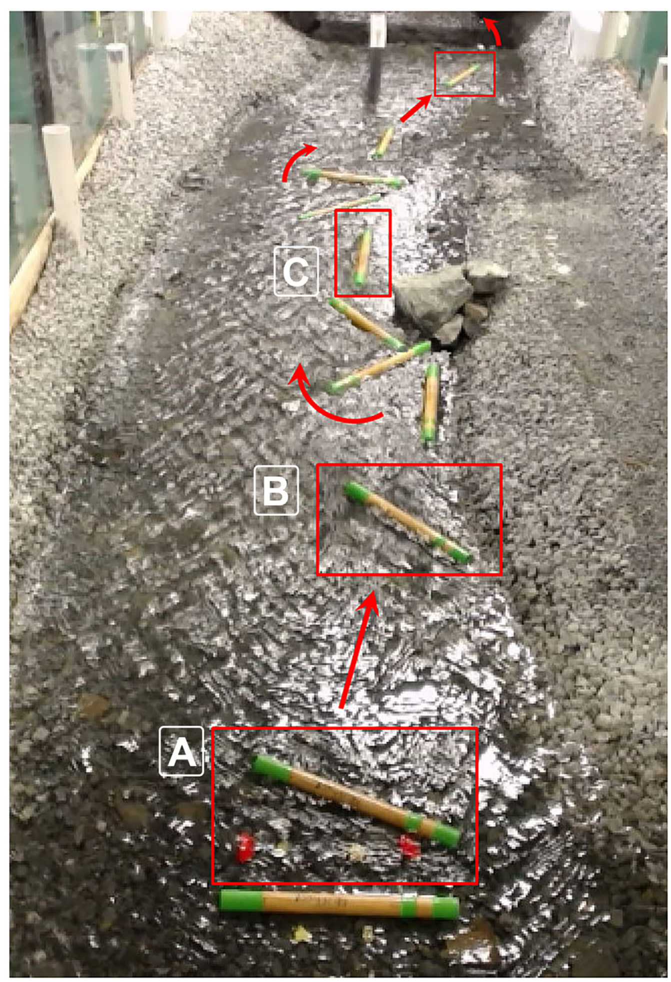

Fig. 10. SmartWood trajectory according video footage, showing starting orientation with recruitment processes (A), rollover and transport processes (B), and interaction of sensor-tagged wood dowel with channel boundaries (C).

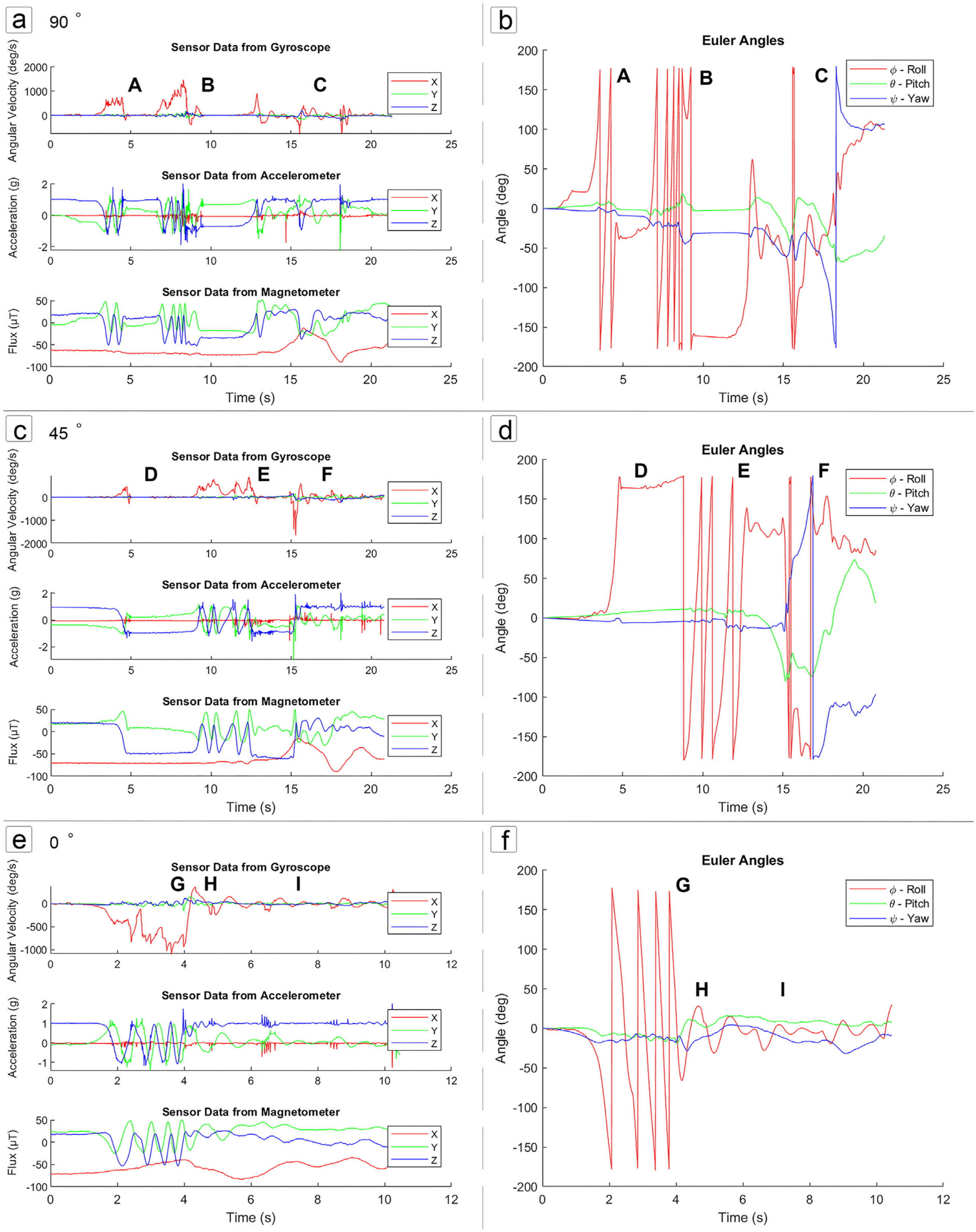

Fig. 11. SmartWood raw data and Euler angle estimates for orientation, starting with an inclination of 90°, 45° and 0° to flow direction.

velocity about the longitudinal axis. The signal started from zero (rest) and maintained a constant velocity for a period of 2 s (compare **A** in Figs. 11a and 12a). As this happened, the acceleration data for the y and z axes indicated a sinusoidal movement relative to gravity. At the same time, the magnetometer recorded a sinusoidal magnetic flux for y and z-axis. Measurements from movement sequence **A** were interpreted as rotational movement around the longitudinal axis, or roll in Euler orientation (Fig. 11b). Our sensor data showed that drag forces imparted by the increasing flow caused the SmartWood dowel to roll over for almost 720°. After the first rolling process, the dowel remained static for a period of 2 s before being remobilised. The SmartWood dowel then continued with another rolling process, **B** (Figs. 11a and 12a), in the direction of the right bank. The rolling process ended after 3.5 rotations with a slight backward rotation when the SmartWood dowel came to rest. Euler angles at this point in time (second 9) indicated a maximal yaw of −46° in the chart, which corresponds with the video footage,

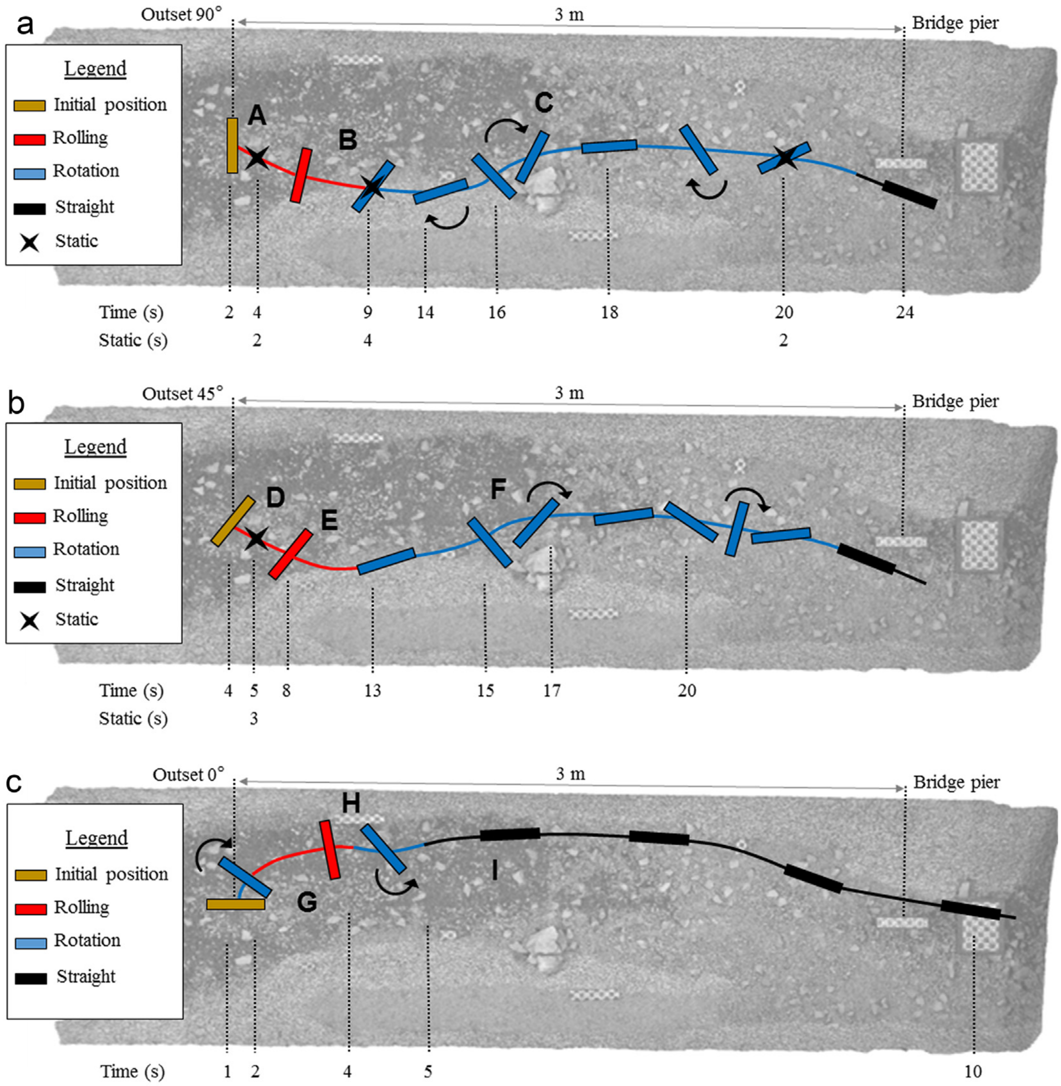

Fig. 12. Experimental SmartWood tracking with an initial start orientation of 90° (a), 45° (b) and 0° (c) to flow direction, showing log trajectory in the scaled stream channel. Flow direction is from left to the right. Red indicates rolling processes (x-axis) and blue shows rotation around the vertical axis (yaw), indicated by arrows. Straight LW movement is displayed in black, and moments of rest are indicated with a cross. The trajectory from initial layout to the bridge pier is 3 m. Significant movement behaviour is indicated with capital letters, from A to I, referring to stages in the raw data and transformed Euler angle records, plotted in Fig. 11, above. (For interpretation of the references to colour in this figure legend, the reader is referred to the web version of this article.)

showing an alignment of 45° with the flow. The sensor-tagged wood dowel remained at this position for about 4 s, before being remobilised and transported downstream. Shortly after an interaction with the right embankment, which was recorded as an impact on the longitudinal axis (second 14.5), the dowel underwent a rotational movement of exactly 180° around the vertical axis. As observed in the sensor data, rotational movement started at negative 30° (second 16) and ended with a yaw of positive 95° (second 20). This resulted in a maximal magnitude for yaw movement of 230°. In comparison with the video record, the sensors showed a discrepancy of approximately 50° against the actual yaw rotation.

At the time of the rotational movement around the z-axis, pitch readings showed a rotation of 70°. Furthermore, a relatively high acceleration force was recorded in the lateral direction: compare sensor data from accelerometer (y-axis, second 18 in Fig. 11a), during the yaw movement in Fig. 12a. The 70° pitch movement, which was not captured in video footage and is physically unlikely, was introduced due to the high acceleration forces during rotational movement, as well as rolling processes of the SmartWood dowel. The video revealed a combination of yaw and pitch. Besides the high lateral acceleration forces, we also identify drift as a possible reason for deviations in Euler orientation. According to the results of our previously conducted verification tests, we observed drift of 1.8 deg·s^{-1} (Table 2). The observed drift of 50° for yaw, suggesting a linear development of drift over time, with a deviation of 0.2 deg·s^{-1}, when considering SmartWood in starting position perpendicular to flow direction and a measuring time of approximately 25 s.

4.2.2. 45° alignment

Data obtained from the 45° alignment to flow direction showed similar movement behaviour as the previous experiment with 90° alignment. The main differences are in shorter resting times for the SmartWood dowel in the channel, and almost continuous movement, involving a 360° rotation after interaction with the right embankment. With increasing discharge, the SmartWood dowel experienced motion around the longitudinal axis. As captured on camera, an approximately 160° rolling process was observed. This movement aligns with the measured and computed sensor data - compare movement sequence **D** in Figs. 11c & d and 12b - followed by a static period of 4 s. SmartWood data captured the remobilisation of the dowel as discharge was further increased, showing four full rotations around the longitudinal axis, compare sequence **E**, with subsequent transport in downstream direction along the right shore. Acceleration and magnetic flux clearly revealed rotational movement around the x-axis (second 9 to 13). Over the first movement stages the sensor-tagged wood dowel was aligned 45° to the flow. Similar to the previously discussed experiment, with a 90° alignment to flow direction as starting condition, the SmartWood dowel interacted with the embankment and experienced an exactly 360° rotation for yaw, according video footage. The movement sequence **F** in Fig. 12b, could be reconstructed via Euler angles (Fig. 11d) from second 15 to 21.

Shortly before the interaction with the embankment the dowel turned from a consistent 45° yaw movement, facing into direction of the channel centre, to 45°, facing the riverbank. At the time of impact, an acceleration signal was measured for the x-axis. After the straight impact, raw data of the SmartWood dowel reveal a high acceleration force in lateral direction of the y-axis (second 15 in Fig. 11c). This lateral acceleration indicates a relatively quick rotational movement, when drag forces on the lateral side of the dowel increase as soon as the dowel becomes aligned perpendicular to the flow. The SmartWood dowel became parallel aligned with the flow after another 315° rotation (video footage). Yaw started at negative 15°, with tendency in positive direction, and finished at negative 110°. The entire movement, according sensor data, leads to an absolute rotation of 265°, which is inconsistent with the estimated yaw from video footage of 405° (90° + 315°). At the same time, however, a significant signal for pitch was computed, showing a maximal amplitude from negative 75° to positive 75°. Total pitch resulted in a magnitude of 150°, which shows the approximate deviation from the estimated rotation of yaw 405°.

As in the first experimental test, the indicated pitch orientation does not match with reality, according to the video footage, and does not show the expected physical movement behaviour. However, a strong signal was measured in acceleration for the y-axis (second 15, second 18), which indicates once more pitch orientation in Euler angles. The interpretation of pitch, as shown in Fig. 11b and d, may be triggered due to the relatively high lateral acceleration forces (y-axis) together with the rolling movement about the longitudinal axis (Fig. 11a and c). Considering merging of yaw and pitch angles for rotational movement around y and z-axis, the observed 180° in yaw from the first experimental test (90° alignment), but also the 405° rotation from the second experimental test (45° alignment) reveal similar outcomes of computed Euler angles and observed movement from video capture for each of the experiments.

4.2.3. 0° alignment

For the third experimental test, the SmartWood was placed with its longitudinal axis aligned in flow direction. As discharge increased, the dowel yawed by 30°, and was then mobilised via rolling. The rolling process, displayed as movement sequence **G** in Fig. 11e, consisted of four full rotations plus an additional 65°, all measured in negative rotational direction. Raw data from the third experimental test (Fig. 11e) showed sinusoidal acceleration of y and z-axis and continuously increasing angular velocity around the longitudinal axis for the mobilisation phase, **G**. This can also be observed in the Euler angle chart (Fig. 11f), with increasing slope of the graph for roll, and decreasing time between the single rotations. The process was interrupted due to interactions between SmartWood and the channel bed, **H**: the graph for acceleration in z direction shows an impact (second 4), leading to (i) a change of dowel alignment in the flume (Fig. 12c), (ii) a reversal of roll with a magnitude of positive 93°, and (iii) a jump in pitch of positive 15° according Euler orientation computation (Fig. 11f). This indicates the end of the mobilisation process where dowel roll was fully transferred to straight movement in the downstream direction, **I**.

As observed in our prior experimental tests, the lateral impact at second 4 triggered a change of pitch orientation. Five seconds after mobilisation the SmartWood dowel was aligned closely to the flow direction and was transported downstream. Yaw, for the interval **I** in Fig. 11f, is consistent with the movement behaviour captured on video, with slight fluctuations in orientation to the left and right. We also observed increasing drift at the beginning of the sensor measurement, similar to our experiences from verification and experimental test obtained and evaluated above. The dowel did not rest at any point in its 2 m trajectory (second 5 to 9), therefore the average speed of the SmartWood dowel was estimated to be 0.5 $m{\cdot}s^{-1}$.

4.3. Key findings

SmartWood allows for the determination of active moving periods (transportation), and depending on pre/post survey opportunities (MacVicar et al., 2009; Ravazzolo et al., 2015), and records from other SmartWood equipped elements, residence times and the nature of stochastic entrainment and terminal ‘hang ups’ can be assessed within the system. However, it is possible that the wood may be ‘at rest’ relative to the local coordinate frame even while drifting down the river, a scenario for which further research into signal conditioning is required. The design of the SmartWood itself can allow for different dimensions and roughness elements, and configurations such as branches and rootwads may be considered, which significantly affect entrainment, transport and accumulation behaviour, similar to the work of Davidson et al. (2015), and Gschnitzer et al. (2017). The following key findings result from our study:

1.) This study provides a proof of concept for the application of 9-DoF smart sensors in a wet, dynamic and impact-prone environment. The smart sensors satisfied our criteria for size, battery life, data storage capacity and processing times for memory download as well as instruction upload. A Wi-Fi connection enabled quick communication with the embedded smart sensor unit at any time throughout our experiments.
2.) Verification tests demonstrated that the data generated from smart sensors meet the measurement requirements, with respect to data accuracy and reliability, for LW experiments in a flume environment. Specifically, the applied smart sensors have shown good sensitivity to movements and impacts, and we were able to accurately reconstruct real-world movements from the sensor data, as verified from experimental observations.
3.) A smart sensor unit was implanted into a wooden dowel, a scale model of LW, for the purpose of movement tracking in a flume environment. Experimental results show that more complex sequences of movement, including simultaneous combinations of yaw, pitch and roll, can be reconstructed from sensor data, as verified using a video record of transport events in the flume.
4.) LW movement pathways, as reconstructed from time integration of sensor data, reveal some deviations from the video record. Rates of drift in the rotation sensor are on the order of 1.8 (± 0.2) $deg{\cdot}s^{-1}$. This results in errors of 3 to 10° for a single roll, pitch and yaw movement (depending on the rate of rotation) throughout our experiments. However, these deviations in rotation measurements, as a function of time, will have to be controlled for, in order to achieve reconstruction of the full LW trajectory.
5.) At a data sampling rate of 100 Hz, it is shown that SmartWood can record impact forces with sufficient resolution to reconstruct LW movements and interactions with channel boundaries and river-crossing infrastructure.

5. Conclusions and outlook

We presented verification and initial experimental tests using smart sensors in wooden dowels, a method that promises to provide novel insights into LW movement behaviour. Verification tests concentrated on quantifying sensor movement under controlled conditions and provided comprehensive data of translational and rotational movement sequences. Experimental tests carried out in a laboratory flume environment are presented, introducing a novel application of SmartWood in LW research. Further verification tests are needed to better understand the limitations of smart sensor measurements, and issues that arise from time-based integration for reconstructing a sequence of movements of LW.

While SmartWood data aligned well with the movements captured through a camera, differences from measured sensor data and captured image data were observed. The sequence of pitch data recorded in the first and second experimental tests does not align with the video images. We believe that orientation estimates are impaired by significant lateral acceleration of the dowels and the drift component. This requires future improvements in computation of orientation estimates, which requires more advanced filtering, as well as zero-velocity-correction for example, in order to subtract gravity and reduce drift. We recommend that further work is needed to (i) evaluate the influence of a steel flume on magnetometer measurements, (ii) compensate drift when integrating raw data for rotation estimates, and (iii) estimate trajectories and obtain information about absolute position at any point of time. To obtain information about absolute position at any point of time, an improved methodology is needed, which can be achieved using a more refined verification procedure, testing SmartWood movement sequences along a predetermined trail. Instead of axes-isolation, as introduced in the present study, a well organised mixture of all axes should be considered for data generation, to be computed with a software algorithm and verified according the actual trajectory. This verification method should be conducted in a non-ferrous environment for more reliable magnetometer data.

Despite the limitations introduced by sensor drift, SmartWood has the potential to be used in further studies, modelling interactions between LW and infrastructure. The SmartWood methodology introduced here allows for future research on entrainment mechanisms, LW transport trajectories, as well as measuring impact forces on channel boundaries, bridge piers and multiple log interactions at existing LW accumulations, respectively. Ultimately, after further development in the laboratory, SmartWood could be applied to in-situ studies. The application of SmartWood will help to better understand LW transport and accumulation processes, both in the field and in the laboratory.

Acknowledgements

The authors acknowledge funding received from the George Mason Centre for the Natural Environment and the Engineering New Zealand Rivers Group.

References

Abbe, T.B., Montgomery, D.R., 2003. Patterns and processes of wood debris accumulation in the Queets river basin, Washington. Geomorphology 51, 81–107.
Ahmad, N., Ghazilla, R.A.R., Khairi, N.M., Kasi, V., 2013. Reviews on various inertial measurement unit (IMU) sensor applications. Int. J. Sig. Process. Syst. 256–262.
Aldoumani, N., Meydan, T., Dillingham, C.M., Erichsen, J.T., 2015. Enhanced Tracking System Based on Micro Initial Measurements Unit to Track Sensorimotor Responses in Pigeons. IEEE, pp. 4.
Assani, A.A., Petit, F., 1995. Log-jam effects on bed-load mobility from experiments conducted in a small gravel-bed forest ditch. Catena 25, 117–126.
Baillie, B.R., Davies, T.R., 2002. Influence of large woody debris on channel morphology in native forest and pine plantation streams in the Nelson region, New Zealand. N. Z. J. Mar. Freshw. Res. 36, 763–774.
Bocchiola, D., Rulli, M.C., Rosso, R., 2006. Flume experiments on wood entrainment in rivers. Adv. Water Resour. 29, 1182–1195.
Braudrick, C.A., Grant, G.E., 2000. When do logs move in rivers? Water Resour. Res. 36, 571–583.
Braudrick, C.A., Grant, G.E., 2001. Transport and deposition of large woody debris in streams: a flume experiment. Geomorphology 41, 263–283.
Davidson, S.L., Mackenzie, L.G., Eaton, B.C., 2015. Large wood transport and jam formation in a series of flume experiments. Water Resour. Res. 51, 10065–10077.
Fischer, C., Sukumar, P.T., Hazas, M., 2013. Tutorial: implementing a pedestrian tracker using inertial sensors. IEEE Pervasive Comput. 12 (2), 17–27.
Geerling, G.W., Labrador-Garcia, M., Clevers, J.G.P.W., Ragas, A.M.J., Smits, A.J.M., 2007. Classification of floodplain vegetation by data fusion of spectral (CASI) and LiDAR data. Int. J. Remote Sens. 28, 4263–4284.
Goseberg, N., Nistor, I., Mikami, T., Shibayama, T., Asce, M., Stolle, J., 2016. Nonintrusive spatiotemporal smart debris tracking in turbulent flows with application to debris-laden tsunami inundation. J. Hydraul. Eng. 142 (12), 17.
Gronz, O., Hiller, P.H., Wirtz, S., Becker, K., Iserloh, T., Seeger, M., Brings, C., Aberle, J., Casper, M.C., Ries, J.B., 2016. Smartstones: a small 9-axis sensor implanted in stones to track their movements. Catena 142, 245–251.
Gschnitzer, T., Gems, B., Mazzorana, B., Aufleger, M., 2017. Towards a robust assessment of bridge clogging processes in flood risk management. Geomorphology 279, 128–140.
Gurnell, A.M., Piegay, H., Swanson, F.J., Gregory, S.V., 2002. Large wood and fluvial processes. Freshw. Biol. 47, 601–619.
Harmon, M.E., Franklin, J.F., Swanson, F.J., Sollins, P., Gregory, S.V., Lattin, J.D., Anderson, N.H., Cline, S.P., Aumen, N.G., Sedell, J.R., Lienkaemper, G.W., Cromack, K., Cummins, K.W., 1986. Ecology of coarse woody debris in temperate ecosystems. Adv. Ecol. Res. 15, 133–302.
Hiller, P.H., Lia, L., Aberle, J., Wirtz, S., Casper, M.C., 2014. Riprap Design on the Downstream Slope of Rockfill Dams - Laboratory Test Rig and Smartstone Sensors. pp. 6.
Hoag, D., 1963. Apollo guidance and navigation considerations of Apollo IMU gimbal lock. In: MIT Instrumentation Laboratory Document E-1344.
Keller, E. A. & Tally, T. 1979. Effects of large organic debris on channel form and fluvial processes in the coastal redwood environment. Ajustments of the Fluvial System. 1979 Proceedings of Tenth Annual Geomorphology Symposium (Ed. by D.D. Rhodes and G.P. Williams), State Univ. of New York, Binghamton, 169–197.
Kok, M., Hol, J.D., Schön, T.B., 2017. Using inertial sensors for position and orientation estimation. Foundations and Trends® in Signal Processing 11, 1–153.
Liu, G.-X., Shi, L.-F., Xun, J.-H., Chen, S., Zhao, L., Shi, Y.-F., 2018. An orientation estimation algorithm based on multi-source information fusion. Meas. Sci. Technol. 29, 115101.
MacVicar, B., Piégay, H., 2012. Implementation and validation of video monitoring for wood budgeting in a wandering piedmont river, the Ain River (France). ESPL 37, 1272–1289.
MacVicar, B.J., PiÃ©Gay, H., Henderson, A., Comiti, F., Oberlin, C., Pecorari, E., 2009. Quantifying the temporal dynamics of wood in large rivers: field trials of wood surveying, dating, tracking, and monitoring techniques. Earth Surf. Process. Landf. 34, 2031–2046.
Madgwick, S.O.H., Harrison, A.J.L., Vaidyanathan, R., 2011. Estimation of IMU and MARG orientation using a gradient descent algorithm. IEEE Int. Conf. Rehabil. Robot. 1–7.
Magnussen, S., Nord-Larsen, T., Riis-Nielsen, T., 2018. Lidar supported estimators of wood volume and aboveground biomass from the Danish national forest inventory (2012–2016). Remote Sens. Environ. 211, 146–153.
Martin, D.J., Harden, C.P., Tran, L., Opavlowsky, R.T., 2018. Investigating patterns of in-channel wood deposition locations in a low gradient, variably-confined alluvial river system. Prog. Phys. Geogr. 42 (2), 139–161.
Milani, G., Volpi, M., Tonolla, D., Doering, M., Robinson, C., Kneubühler, M., Schaepman, M., 2018. Robust quantification of riverine land cover dynamics by high-resolution remote sensing. Remote Sens. Environ. 217, 491–505.
Nakamura, F., Swanson, F.J., 1994. Distribution of coarse woody debris in a mountain stream, western Cascade Range, Oregon. Can. J. Fish. Aquat. Sci. 24, 9.
Olinde, L., Johnson, J.P.L., 2015. Using RFID and accelerometer-embedded tracers to measure probabilities of bed load transport, step length, and rest times in mountain stream. Water Resour. Res. 51 (9), 7572–7589.
Phillips, C., Marden, M., Basher, L.R., 2018. Geomorphology and forest management in New Zealand's erodible steeplands: an overview. Geomorphology 307, 107–121.
Piegay, H., Thevenet, A., Citterio, A., 1999. Input storage and distribution of large woody debris along a mountain river continuum the Drome River, France. Catena 35, 19–39.
Ravazzolo, D., Mao, L., Picco, L., Lenzi, M.A., 2015. Tracking log displacement during floods in the Tagliamento River using RFID and GPS tracker devices. Geomorphology 228, 226–233.
Richardson, J.J., Moskal, L.M., 2016. An integrated approach for monitoring contemporary and recruitable large woody debris. Remote Sens. 8, 13.
Ruiz-Villanueva, V., Piegay, H., Gaertner, V., Perret, F., Stoffel, M., 2016a. Wood density and moisture sorption and its influence on large wood mobility in rivers. Catena 140, 182–194.
Ruiz-Villanueva, V., Wyżga, B., Zawiejska, J., Hajdukiewicz, M., Stoffel, M., 2016b. Factors controlling large-wood transport in a mountain river. Geomorphology 272, 21–31.
Ruiz-Villanueva, V., Bürkli, L., Mazzorana, B., Mao, L., Ravazzolo, D., Iribarren, P., Wohl, E., Nakamura, F., Stoffel, M., Rivière, N., Paquier, A., 2018. Defining and characterizing wood-laden flows in rivers using home videos. E3S Web Conf. 40, 02014.
Rusyda, M.I., Hashimoto, H., Ikematsu, S., 2014. Log jam formation by an obstruction in a river. In: River Flow 2014, pp. 717–724.
Schenk, E.R., Moulin, B., Hupp, C.R., Richter, J.M., 2014. Large wood budget and transport dynamics on a large river using radio telemetry. Earth Surf. Process. Landf. 39, 487–498.
Smikrud, K.M., Prakash, A., 2006. Monitoring large woody debris dynamics in the Unuk River, Alaska using digital aerial photography. GISci. Remote Sens. 43, 142–154.
Stubblefield, A.P., Reuter, J.E., Goldman, C.R., 2009. Sediment budget for subalpine watersheds, Lake Tahoe, California, USA. Catena 76, 163.172.
Tempelman, E., Dwaikat, M.M.S., Spitás, C., 2012. Experimental and analytical study of free-fall drop impact testing of portable products. Exp. Mech. 52, 1385–1395.
Tonon, A., Picco, L., Rainato, R., 2018. Test of methodology for developing a large wood budget: a 1-year example from a regulated gravel bed river following ordinary floods. Catena 165, 115–124.

Valyrakis, M., Farhadi, H., 2017. Investigating coarse sediment particles transport using PTV and “smart-pebbles” instrumented with inertial sensors. EGU General Assembly Conference 19, 9980.
Wohl, E., Jaeger, K., 2009. A conceptual model for the longitudinal distribution of wood in mountain streams. Earth Surf. Process. Landf. 34, 329–344.
Worsey, M.T., Espinosa, H.G., Shepherd, J.B., Thiel, D.V., 2019. Inertial sensors for performance analysis in combat sports: a systematic review. Sports (Basel) 7.
Wyżga, B., Mikuś, P., Zawiejska, J., Ruiz-Villanueva, V., Kaczka, R.J., Czech, W., 2017. Log transport and deposition in incised, channelized, and multithread reaches of a wide mountain river: tracking experiment during a 20-year flood. Geomorphology 279, 98–111.
Xu, T., Sheng, X., Zhang, T., Liu, H., Liang, X., Ding, A., 2018. Development and validation of dummies and human models used in crash test. Appl. Bionics Biomech. 2018, 3832850.
Yin, L., Wang, X., Ni, Y., Zhou, K., Zhang, J., 2018. Extrinsic parameters calibration method of cameras with non-overlapping fields of view in airborne remote sensing. Remote Sens. 10, 1298.